


Criterion for particle rebound during wet collisions on elastic coatings

Matthew Ryan Tan,¹ Yumo Wang,^{1,2,*} and Joelle Frechette ^{1,†}

¹*Department of Chemical and Biomolecular Engineering, Hopkins Extreme Materials Institute, Johns Hopkins University, Baltimore, Maryland 21218, USA*

²*National Engineering Laboratory for Pipeline Safety, Beijing Key Laboratory of Urban Oil and Gas Distribution Technology, China University of Petroleum, Beijing, 18# Fuxue Road, Changping District, Beijing 102249, China*



(Received 24 December 2018; published 23 August 2019)

We combine lubrication theory and solid linear elasticity to model the elasto-hydrodynamic deformation of a rigid, spherical particle impacting a stratified surface—a soft incompressible coating atop a rigid substrate. The model depends on three dimensionless parameters: Stokes number, elasticity parameter, and thickness parameter. These parameters collectively determine whether the particle will stick to or rebound against the stratified surface. We show that coating thickness moderates the degree to which elasticity affects the rebound criteria (and vice versa) in a fashion distinct from the effect of the elasticity or of the Stokes number. We also demonstrate the possibility of approximating a stratified surface as an elastic half space with an elasticity between the rigid substrate and soft coating. This “effective elasticity” of the half space couples both the elasticity parameter and thickness parameter of the stratified surface condition while maintaining the same sticking criteria. Lastly, we discuss the limitations of this effective elasticity, such as in thin or more-rigid coatings.

DOI: [10.1103/PhysRevFluids.4.084305](https://doi.org/10.1103/PhysRevFluids.4.084305)

I. INTRODUCTION

Wet particle-particle or particle-wall collisions play an important role in many natural and industrial phenomena, including particle deposition [1], erosion [2], and wet granular flows [3,4]. For processes with particulate and multiphase systems, a better understanding of particle-particle and particle-wall collisions is important for the modeling and optimization of fluid flow and particle transport, for example, in riser reactors [5,6], impurity separators [7], and pipelines [8]. Beyond its industrial applications, colloidal and particle-wall interactions in biological microenvironments can lead to technical advances in pharmaceutical applications like drug delivery [9], blood substitutes [10], and biomimetics [11,12], as the microenvironment *in vivo* consists of a large variety of particles and boundaries (protein, cells, vessels, bones, and tissues) where drainage and wet collisions can occur.

For particle-particle or particle-wall collisions mediated by a viscous fluid, the kinetic energy of the colliding particles is dissipated into the fluid through viscous forces. Simultaneously, viscous forces can cause elastic deformation of the interacting surfaces [13–15], thereby increasing the fluid gap width, decreasing the rate of fluid drainage, and decreasing the rate of viscous dissipation [16]. Therefore, the interplay between elastic deformation and viscous forces determines the ratio of energy conservation and dissipation during particle collision. For instance, in the case of a wet

*ywang@cup.edu.cn

†jfrechette@jhu.edu

collision between perfectly rigid surfaces, the absence of a deformable boundary leads to completely inelastic collisions. On the other hand, compliant boundaries allow partially inelastic collisions, or elasto-hydrodynamic bouncing [17]. Therefore, understanding the role of elastic deformation in wet particle collisions is crucial in predicting the dynamics of soft particulate systems.

The problem of elasto-hydrodynamic collisions has been thoroughly studied over the years. Davis, Serayssol, and Hinch [18] (DSH) developed a framework for elasto-hydrodynamic bouncing and showed that collisions were dependent on two dimensionless parameters: the Stokes number St and elasticity ε . Experiments wherein spheres of various elasticities were dropped onto liquid films atop glass [19,20] showed good agreement with DSH theory. In particular, bouncing was observed to occur only when the Stokes number exceeded a critical Stokes number, St_c . Moreover, the wet coefficient of restitution COR_{wet} , defined as the ratio between a particle's velocities immediately after and before the collision, is an important required parameter in discrete elements method simulation of particulate flows [21,22]. The COR_{wet} depends on the Stokes number and its critical value, St_c [17,23,24]. Following the seminal work of DSH, many variations and extensions of the original elasto-hydrodynamic bouncing problem have been studied. For example, oblique collisions and the effect of impact angle on St_c have been investigated using pendulum configurations [24–26]. Müller and Huang [27] examined how the fluid film thickness atop the glass substrate would affect COR_{wet} . Surface asperities have also been demonstrated to significantly impact St_c and, consequently, the wet coefficient of restitution [24]. Chastel *et al.* [28] further investigated the effect of asperities on bouncing by analyzing the collision against a fabricated microtextured surface with various heights and surface fractions of micropillars and found the critical Stokes number to be significantly influenced by surface texture.

A limit that remains in the description of elastic collisions is that particles are generally assumed to be homogeneous. The elasto-hydrodynamic deformation during bouncing is, therefore, determined solely based on bulk material properties. Stratified particles, more specifically, rigid particles with soft coatings, are ubiquitous [29,30]. Nevertheless, the role of stratification on elasto-hydrodynamic bouncing is not well-understood, especially considering that stratification influences elasto-hydrodynamic deformation for other configurations. For instance, Mahadevan *et al.* analyzed the sliding motion of particles past a stratified substrate and clarified the role played by the coating thickness [31]. Leroy and Charlaix [32] and Restagno *et al.* [33] modeled an immersed spherical probe oscillating some distance away from either a thin or a thick, substrate-bounded elastic film. They then showed through models and experiments how to use elasto-hydrodynamics to obtain the mechanical properties of a compliant layer from out-of-contact oscillations. Craster *et al.* presented the numerical results for the gravitational settling of a two-dimensional (2D) object toward a plane wall with a soft coating in a viscous fluid [34]. Wang *et al.* [35,36] studied elasto-hydrodynamic deformation in the context of dynamic surface forces measurements. They observed that dynamic surface forces depend on the mechanical properties and coating thickness. They also showed that simple corrections for stratification employed to predict the deformation caused by a spherical indenter were not sufficient to account for the role of the coating thickness on the deformation during dynamic surface force measurements. These recent advances demonstrate the noninterchangeable role played by coating elasticity and thickness on the elasto-hydrodynamic problem. However, due to the complex nature and nonlinearity of the governing equations [37,38], full numerical calculations are necessary to fully describe the variation in fluid gap thickness and deformation profile of the soft layer during the process of approaching or bouncing, which consume intensive computational source and time.

Here we analyze the bouncing of a rigid particle off a stratified coating in viscous fluid (see Fig. 1). We model the full elasto-hydrodynamic bouncing process through the incorporation of three governing equations coupling the fluid drainage and infusion, the elastic deformation, and the particle motion, and solve the equations numerically. We show the transition from thick to thin coating thickness on the dynamics of the fluid gap profile and particle velocity for a fixed Stokes number and elasticity. From an energy analysis, we investigate the relationship between hydrodynamic force and the soft coating's stored elastic energy. We compare the evolution of the

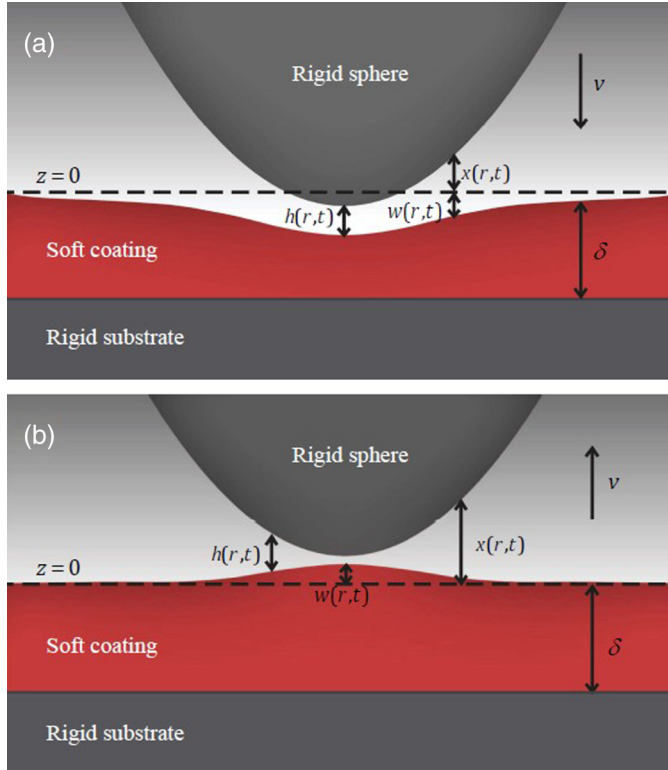


FIG. 1. Schematic diagram showing the (a) approach and (b) bouncing of a spherical particle against a coated substrate. Important variables include the fluid gap width (h), the undeformed separation (x), the deformation (w), particle velocity (v), and coating thickness (δ). The particle is immersed in a Newtonian fluid with viscosity (η). In (a) as the particle approaches the soft coating, fluid is drained out of the gap. In (b) fluid is infused into the gap as the particle rebounds away from the coating. The figure is scaled such that the horizontal axis (radial direction) is compressed 50 times relative to the vertical axis (z direction), which results in the nonspherical appearance of the particle.

particle’s kinetic energy and the soft coating’s elastic energy and show that, depending on the coating thickness, the energy transfer between the particle and the soft coating repeatedly transitions between a viscous-dominated and elastic-dominated regime. Lastly, we define an effective elasticity parameter that couples thickness and elasticity while maintaining the same rebound characteristics.

We provide a close form correction for the St_c in terms of an effective elasticity that accounts for the effect of stratification. The correction can be employed along existing classic scaling of St_c with surface elasticity from Davis *et al.* [18] and Lian *et al.* [39] or empirical curves [40] developed for homogeneous particles, without the need of full numerical simulations. Aiming to further simplify the original problem, we couple the coating thickness and elasticity parameters into one single effective elasticity, and therefore reduce the dependency on three dimensionless parameters to only two (St and ε). This effective elasticity is different from the one conceptualized by Wang *et al.* [35] since St_c is independent of time and space, unlike the deformation and fluid gap profile. Therefore, it is possible to use the effective elasticity to realign the St_c between configurations with different coating thicknesses. This method could contribute to improving the accuracy of large-scale multiparticle simulations, which are currently limited to the dichotomous “hard sphere” or “soft sphere” particles [21], with limited options for stratified materials. We also provide regime maps that can be employed to predict rebound or sticking after normal collisions, which are useful in

understanding how clusters or aggregation initiate. Our work also has implications for the studies of some non-Newtonian behavior of highly concentrated particulate systems [41], including shear thickening, for which the detailed mechanism is still under debate [42–44].

II. THEORETICAL DEVELOPMENT

A. Description

We pose the problem as follows: a spherical particle of radius a and mass m approaches a wall coated with compliant film of thickness δ and elastic modulus E , as shown in Fig. 1. Cylindrical coordinates are chosen due to the radial symmetry of the problem. The origin is fixed at the point on the coating surface (undeformed) that is closest to the spherical particle. At time $t = 0$, the sphere and coating are separated by an undeformed gap of width x_0 by a Newtonian fluid of dynamic viscosity η . Initially, the velocity of the sphere is v_0 and the momentum of the sphere is therefore mv_0 , directed perpendicular toward the wall (see Fig. 1).

A force balance governs the overall motion of the spherical particle:

$$F_H = \int_0^a 2\pi r p(r) dr = m \left[\frac{\partial^2 h(0, t)}{\partial t^2} - \frac{\partial^2 w(0, t)}{\partial t^2} \right]. \quad (1)$$

In Eq. (1), $p(r)$ is the pressure distribution within the fluid gap, h is the fluid gap thickness, w is the coating deformation, r is the radial coordinate, and t is time. The integral term is the hydrodynamic force that resists the motion of the spherical particle, while the derivative term is the product of the mass and the instantaneous acceleration of the particle. If we assume the fluid gap is small relative to the sphere radius ($x_0/a \ll 1$), together with a no-slip condition on both surfaces and continuum fluid phase, the pressure within the thin fluid gap can be modeled with the lubrication equation:

$$\frac{\partial h(r, t)}{\partial t} = \frac{1}{12\eta r} \frac{\partial}{\partial r} \left[r h^3 \frac{\partial p(r, t)}{\partial r} \right]. \quad (2)$$

The lubrication approximation also requires the inertial terms of the fluid in the Navier-Stokes equation to be relatively small compared to the viscous term. For the current geometry, this condition can be stated as $\text{Re} \ll a/x_0$, in which Re is the Reynolds number defined as $\text{Re} = \rho_f v_0 a / \eta$ with ρ_f the fluid density. In the lubrication limit, the fluid pressure decreases radially in the r direction but does not vary with the z direction.

We can obtain the coating deformation using the fluid pressure from the lubrication equation. The pressure directly translates to a normal stress boundary condition on the compliant layer at $z = 0$. The other boundary of the compliant layer located at $z = -\delta$ is attached to a rigid substrate under a sticky boundary assumption. With these boundary conditions, we calculate the deformation of the compliant coating using the equations from Leroy and Charlaix [32], where the linear elastic theory of soft coatings in contact mechanics developed by Gacoin *et al.* [45] was applied to the context of elastohydrodynamic oscillations. The deformation of the compliant coating at $z = 0$ is given by

$$w(r, t) = \int_0^\infty \frac{2}{E^* \xi} X(\xi \delta) Z(\xi) J_0(\xi r) d\xi; \quad E^* = E/(1 - \nu^2), \quad (3)$$

where

$$X(\xi \delta) = \frac{\gamma(1 - e^{-4\xi\delta}) - 4\xi\delta e^{-2\xi\delta}}{\gamma(1 + e^{-4\xi\delta}) + [\gamma^2 + 1 + 4(\xi\delta)^2]e^{-2\xi\delta}}; \quad \gamma = 3 - 4\nu, \quad (4)$$

and

$$Z(\xi) = \xi \int_0^\infty r p(r, t) J_0(\xi r) dr. \quad (5)$$

In Eqs. (3)–(5), E^* is the reduced Young’s modulus, J_0 is the zeroth-order Bessel function, ν is the Poisson’s ratio of the coating, δ is the coating thickness, ξ is the Hankel transform variable, and $w(r)$ is the normal deformation profile of the coating at the surface. To determine if the strain in the coating remains within the linear elasticity regime, we estimate the strain as $\sqrt{w(0,t)}/a$ [46], which does not exceed $0.6\sqrt{x_0/a}$. The 0.6 term is extracted from our simulation data, while the term within the radical stems from the scaling of coating deformation [see Eqs. (10) and (11) below]. Given that the term within the radical is $\ll 1$, the strain does not exceed the linear elasticity limit, so deformation can be calculated using the biharmonic equation. With an expression for the coating deformation $w(r, t)$, the fluid film thickness, $h(r, t)$, can be now described as

$$h(r, t) = x(0, t) + \frac{r^2}{2a} + w(r, t). \quad (6)$$

In Eq. (6), $x(0, t)$ is the central undeformed position at time t , and r is the radial position from the center (see Fig. 1). We use a parabolic approximation to model the central gap between a sphere and a planar surface that are near contact. With the equations for $h(r, t)$ and $w(r, t)$, we can complete the force balance on the sphere [Eq. (1)].

The configuration described above is one of the geometries relevant to elasto-hydrodynamic collisions. Our analysis focuses on the sphere-wall configuration, which is commonly employed in particle-rebound experiments [19,20,47]. In the configuration investigated here, only the rigid wall is coated with a compliant film, while the sphere’s surface is not. Note, however, that the analysis presented can be generalized to other configurations. The same equations can be used to model a sphere-sphere collision by replacing our sphere radius with a “reduced radius” parameter that factors the radii of both spheres [18]. Alternatively, if it were the sphere instead of the rigid wall that was coated with compliant film, the equations and boundary conditions would remain unchanged, but if the coating were applied to both the sphere and the rigid wall, the deformation of each coating should be summed together for the force balance [48].

B. Nondimensionalization

We rely on our previous nondimensionalization to rescale Eqs. (1)–(6) and extract three key nondimensional parameters [35]. The normal characteristic separation is the initial undeformed gap width, x_0 , and the radial characteristic length is set to be the hydrodynamic radius, $\sqrt{ax_0}$. The characteristic timescale is set to be x_0/v_0 , the time it takes the sphere to touch the planar surface if it traveled at its constant initial velocity. We introduce these dimensionless parameters into Eq. (2) and rearrange the equation. The resulting dimensionless form of the lubrication equation is

$$\frac{\partial \hat{h}}{\partial \hat{t}} = \frac{1}{12\hat{r}} \frac{\partial}{\partial \hat{r}} \left(\hat{r} \hat{h}^3 \frac{\partial \hat{p}}{\partial \hat{r}} \right), \quad (7)$$

where the dimensionless variables are

$$\hat{h} = h/x_0, \quad \hat{t} = \frac{v_0}{x_0} t, \quad \hat{r} = r/\sqrt{ax_0}, \quad \hat{p} = \frac{x_0^2}{a\eta v_0} p, \quad \hat{v} = \frac{v}{v_0}. \quad (8)$$

From Eqs. (3)–(5), the scaling parameter for the Hankel transform variable ξ is $1/\sqrt{ax_0}$, since the multiplication of ξ and r in the Bessel function should be rendered dimensionless. The dimensionless coating thickness T is therefore $\delta/\sqrt{ax_0}$, since $\xi\delta$ appears as an exponential order in Eq. (4). The scaling parameter for the deformation $w(r, t)$ is also set to be x_0 , the same as for $h(r, t)$, since the deformation is subtracted directly from $h(r, t)$. The corresponding dimensionless equation for the elastic deformation is then derived as

$$\hat{w}(\hat{r}, \hat{t}) = \varepsilon \int_0^\infty \frac{2}{\hat{\xi}} X(\hat{\xi} T) \hat{Z}(\hat{\xi}) J_0(\hat{\xi} \hat{r}) d\hat{\xi}, \quad (9)$$

with the dimensionless variables obtained being

$$\hat{\xi} = \xi \sqrt{ax_0}, \quad T = \delta / \sqrt{ax_0}, \quad \hat{w} = w/x_0, \quad \hat{Z} = \frac{1}{\eta v_0} \left(\frac{x_0}{a} \right)^{1.5} Z, \quad \varepsilon = \frac{\eta v_0 a^{1.5}}{E^* x_0^{2.5}}. \quad (10)$$

Note that the elasticity parameter ε , which is derived directly from the nondimensionalization of Eq. (3), serves as a measure for the compliance of the coating material under current conditions (η, a, v_0, x_0). Lastly, the dimensionless force balance on the sphere can be derived as

$$\hat{F}(\hat{t}) = \text{St} \left[\frac{\partial^2 \hat{h}(0, \hat{t})}{\partial \hat{t}^2} - \frac{\partial^2 \hat{w}(0, \hat{t})}{\partial \hat{t}^2} \right] = \frac{1}{3} \int_0^{\sqrt{a/x_0}} \hat{p}(\hat{r}, \hat{t}) \hat{r} d\hat{r}, \quad \text{St} = \frac{m v_0}{6\pi \eta a^2}. \quad (11)$$

In Eq. (11) we neglect gravitational force. Gravitational forces can be neglected when the initial kinetic energy is greater than the initial gravitational energy, i.e., when $\frac{\Delta \rho g x_0}{\rho_s v_0^2} \ll 1$. Based on Eqs. (7)–(11), the change in the sphere velocity, coating deformation, separation, and other variables during approach and rebound is determined by three dimensionless parameters—Stokes number St , elasticity ε , and coating thickness T . For comparison, approach and rebound on a half-space coating are described with analogous dimensionless parameters St and ε [18]. The addition, here, of the third parameter T accounts for the constraints in the coating deformation due to finite thickness effects caused by stratification. In addition, the Poisson's ratio is a fourth parameter, which cannot be decoupled from Eq. (3) because of its nonlinear dependence with $X(\xi\delta)$. An alternative approach to disentangle $X(\xi\delta)$ and derive simpler formulation of Eq. (9) would be using polynomial approximations for $X(\xi\delta)$, which are only valid for either thin or thick coatings. To capture the role of the coating thickness, especially the transition between thin to thick films (which includes intermediate film thicknesses), we instead opted to use here a fixed Poisson's ratio of $\nu = 0.5$, which encompasses many polymeric materials and rubbers [49]. Elastohydrodynamic deformation for compressible materials ($\nu < 0.5$) has been investigated in Ref. [30]. Based on Ref. [30], we do not expect the choice of the Poisson's ratio to affect the bouncing of a rigid sphere from a thick coating. For thinner coatings we expect that compressibility will increase the normal deformation and reduce the effect of the constraint imposed by the rigid substrate (for a given St and ε).

To solve Eqs. (7), (9), and (11), we use a numerical algorithm that extrapolates changes in the fluid gap at small time increments. First, at $\hat{t} = 0$, we use 500 evenly spaced points to discretize the fluid gap in the central region ($\hat{r} < 0.1\sqrt{a/x_0}$) of the sphere, where non-negligible deformation will occur. We then make an estimate of the fluid gap after a small time increment ($\Delta\hat{t} = 0.02$) based on the instantaneous sphere velocity. The change in the fluid gap is used to calculate the fluid pressure based on the lubrication equation [Eq. (7)]. With the fluid gap pressure, we use the biharmonic equation of linear elasticity [Eq. (9)] to solve for the coating deformation. We also integrate the fluid gap pressure to get the hydrodynamic force [Eq. (11)]. For $0.1\sqrt{a/x_0} < \hat{r} < \sqrt{a/x_0}$ we use an approximation for the pressure, $\hat{p}(\hat{r}, \hat{t}) = 3\hat{v}/(\hat{h} - \varepsilon\hat{w} + \hat{r}^2/2)^2$ [18] with the underlying assumption that the deformation is sufficiently small that it does not affect the pressure. With the updated deformation profile and hydrodynamic force, we can calculate the expected fluid gap profile from Eq. (11). Next, we compare the calculated fluid gap profile to the estimated value. If the difference in fluid gap at all points throughout the mesh does not exceed 0.0001, we consider the fluid gap profile to satisfy the differential equations, and proceed to the next time increment. If not, we calculate the weighted arithmetic mean of the estimated (weight = 0.9) and calculated (weight = 0.1) fluid gap profile. The mean value is used as the new estimated fluid gap for the next iteration, and this cycle continues until convergence. We do not consider surface forces, such as van der Waals interactions, in our algorithm because we are solely interested in the contribution of elastohydrodynamic deformation to the sticking behavior of the falling spheres. However, should the fluid gap become extremely narrow (<50 nm), such surface forces will become important. In those cases, the van der Waals and electrostatic double layer interactions can be incorporated into the boundary stress condition of the elastic layer to modify the algorithm.

III. RESULTS AND DISCUSSION

In the following sections, Secs. II A and III B, we set $St = 5$ and $\varepsilon = 0.01$ to analyze the effect of coating thickness T separately from the two other dimensionless parameters. The choice of Stokes number and elasticity is such that our results can be compared to those of Davis *et al.* [18]. Furthermore, under these conditions, changing the coating thickness will result in either bouncing or sticking behaviors, as opposed to a smaller elasticity parameter or Stokes number, where there might not be bouncing regardless of the thickness parameter. We investigate three different regimes for the thickness parameter: thin ($T < 0.1$), intermediate ($0.1 < T < 1$), and thick ($T > 1$). We provide an animation in the Supplemental Material [50] that compares the approach, deformation, and rebound for the four particular thickness parameters: $T = 0.05, 0.5, 5$, and 50 .

A. Fluid drainage and infusion during approach and rebound

To investigate the effect of coating thickness on the fluid drainage and infusion, we track three variables: the central fluid gap $\hat{h}(0, \hat{t})$, the coating deformation at the center $\hat{w}(0, \hat{t})$, and the sphere velocity $\hat{v}(\hat{t})$; see Figs. 2(a)–2(c). We evaluate the change in these three variables, during the sphere’s approach and rebound, for thin ($T = 0.05$), intermediate ($T = 0.5$), and thick ($T = 5, 50$) coatings. In Fig. 2(a), our results for the central fluid gap for the thinnest coatings ($T = 0.05$) closely match the Reynolds lubrication theory where, as the central fluid gap decreases, the sphere decelerates to a stop and does not rebound. Due to the mechanical constraint of the rigid substrate supporting the very thin coating, the coating deformation at the center is negligible. On the other hand, for the thickest coating ($T = 50$), our results for the central fluid gap are also in close agreement with DSH half-space results [18]. DSH also noted similar oscillatory motion in the sphere velocity of their half-space model, indicating alternating approach and rebound phases [18]. For the thick coating condition, the amplitude of the coating deformation at the center is large compared to that of the thin coating. Furthermore, the coating deformation also reverses sign. A comparison of the coatings with deformations of opposite signs during approach and rebound is illustrated in Fig. 1. Based on our sign convention, Figs. 1(a) and 1(b) display positive and negative coating deformations, respectively.

First, we explain the effect of T on the coating deformation shown in Fig. 2(b). Coating compliance is the ratio of the coating displacement to the applied stress. Under a given applied stress, the magnitude of the deformation will be larger if the coating is more compliant [51]. Coating compliance is dependent on both ε and T parameters. The relationship between the elasticity parameter ε and compliance is straightforward since the elastic modulus of the coating is included within the parameter. Because the coating is bound to the substrate, the thickness parameter T also similarly affects the compliance of the coating. The compliance of thin coatings decreases and can even become comparable to that of the underlying substrate, while compliance of thicker coatings is more dependent on the elastic properties of the coating itself. In our scenario, since we have a rigid underlying substrate, the compliance decreases as the coating thickness decreases. Another consequence of stratification is that the elastic properties of the coating (included in ε) have less effect on the coating compliance as the thickness parameter decreases. Given the same pressure distribution, a thicker coating will deform more than a thinner coating, which corresponds to the higher amplitudes in Fig. 2(b). The mechanical constraints from the underlying substrate also explain why the deformation at $\hat{t} = 0$ varies even when all other initial conditions (ε and St), are identical.

The changes in coating compliance caused by a decrease in the coating thickness also affect the central fluid gap [$\hat{h}(0, \hat{t})$; see Fig. 2(a)], which is indicative of the rate of fluid drainage and infusion. A downward slope corresponds to fluid drainage, while an upward slope corresponds to fluid infusion at the center. Note that the drainage or infusion at the center does not necessarily imply that the particle as a whole is approaching or rebounding (more details in Fig. 3). We can distinguish between drainage and infusion by defining $\hat{t}_{h\min}$, the time wherein the central fluid gap

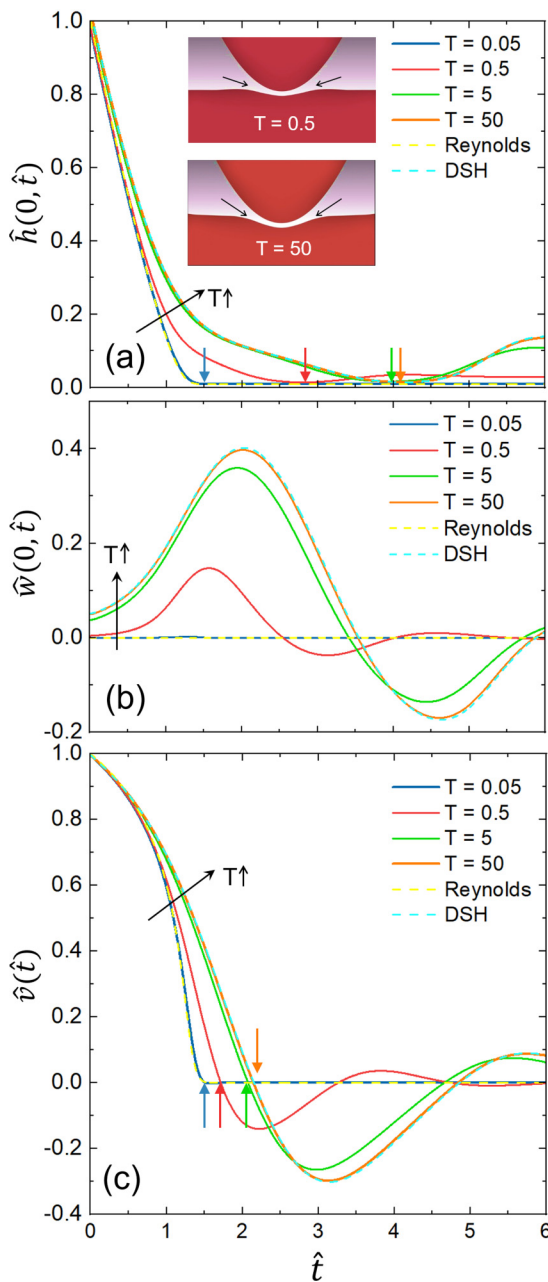


FIG. 2. From top to bottom: (a) Central fluid gap width $\hat{h}(0, \hat{t})$, (b) central coating deformation $\hat{w}(0, \hat{t})$, and (c) particle velocity $\hat{v}(\hat{t})$ during the collision of a spherical particle against a stratified, flat surface. Stokes number and elasticity of the film are held constant at $St = 5$ and $\varepsilon = 0.01$. The four chosen thickness parameters encompass the thin ($T = 0.05$), intermediate ($T = 0.5$), and thick ($T = 5, 50$) regimes for coating thicknesses. The DSH and Reynolds limit for a half space and foundation, respectively, are included as dashed lines. Arrows in (a) mark the first transition from fluid drainage to infusion at the center, while arrows in (c) mark the first transition from the particle's approach to rebound. Inset in (a): Pathway for fluid infusion into the central gap for intermediate and thick coatings, $T = 0.5$ (left) and $T = 50$ (right), respectively. When the deformation of the coating adopts a curvature similar to that of the particle, the narrowness of the fluid gap at the sides determines the rate of fluid infusion into the gap.

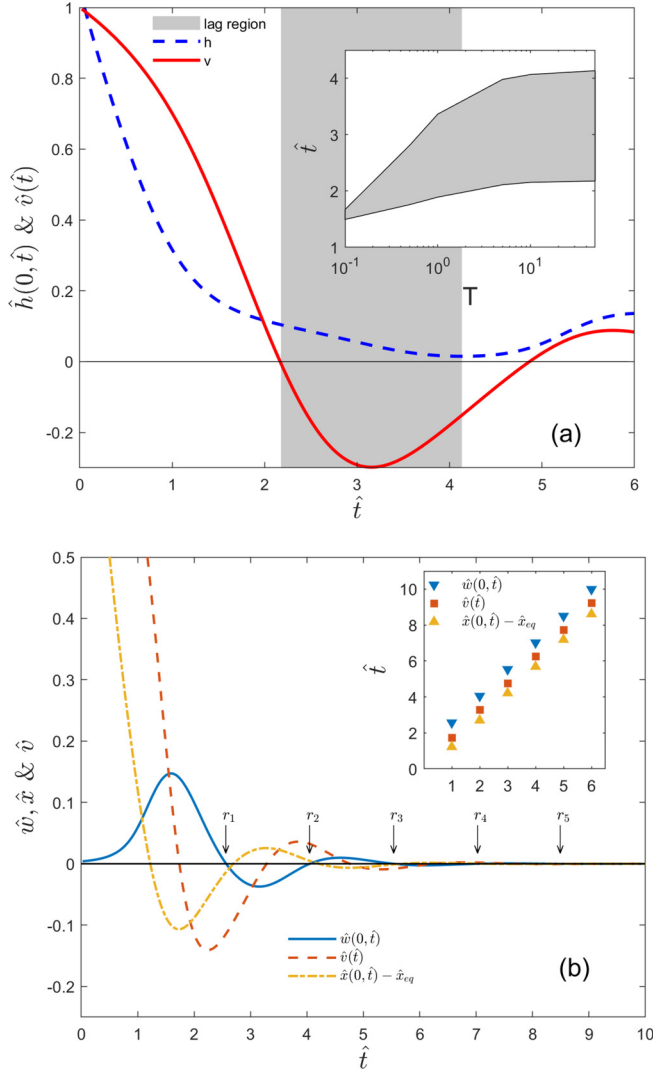


FIG. 3. (a) Comparison between the dimensionless velocity (solid line) of the sphere and the dimensionless central gap (dashed line) for $St = 5$, $\varepsilon = 0.01$, and $T = 50$. The lag region (gray) is between $\hat{t}_{v=0}$ and $\hat{t}_{h\min}$. Inset: $\hat{t}_{v=0}$ and $\hat{t}_{h\min}$ for $St = 5$, $\varepsilon = 0.01$, and different thickness parameters. (b) Comparison between the velocity of the sphere, the central coating deformation, and the central undeformed gap for $St = 5$, $\varepsilon = 0.01$, and $T = 0.05$. The undeformed gap is adjusted by subtracting \hat{x}_{eq} so that it oscillates around the x axis. Intersections between the central coating deformation (blue) and the x axis (black line) are marked with r_i . Inset: The first through sixth time \hat{t} each of the curves crossed the x axis.

is most narrow, indicated with the arrows in Fig. 2(a). Fluid drainage and infusion occur mostly before and after $\hat{t}_{h\min}$, respectively. There are two notable trends in Fig. 2(a): (1) The rate of central fluid drainage decreases as T increases, and (2) $\hat{t}_{h\min}$ increases with T . The reason behind (1) is that as the coating compliance increases with T , the increased deformation of the coating widens the fluid gap, which in turn reduces the necessity for fluid drainage. (2) is a consequence of the differences in velocity profiles in Fig. 2(c) discussed below.

Deceleration of the spherical particle is dependent on the size of the fluid gap. As the fluid gap decreases, the lubrication pressure and hydrodynamic force increase within the interstitial gap.

The hydrodynamic force opposes the motion of the sphere, resulting in the deceleration of the particle, as shown in Fig. 2(c). As the coating compliance increases with T , the magnitude of the coating deformation also increases, resulting in a wider fluid gap. Therefore, a wider fluid gap decreases the hydrodynamic force, thereby reducing the rate of deceleration of the spherical particle. Consequently, the particle can move toward the coating for a longer period of time, which increases the time until the fluid gap is minimum $\hat{t}_{h \min}$.

By aligning Figs. 2(a)–2(c) vertically, we can compare features among the three sets of curves. For example, we define $\hat{t}_{v=0}$ as the first time point wherein the velocity is zero, which we mark with arrows in Fig. 2(c). For intermediate and thick coatings, the peak of coating deformation in Fig. 2(b) closely corresponds to $\hat{t}_{v=0}$ in Fig. 2(c). As the particle decelerates significantly and almost no longer moves toward the soft coatings, the lubrication pressure starts to drop [Eq. (1)]; therefore the coating will start to return to its uncompressed state, thereby decreasing the magnitude of the deformation. On the other hand, $\hat{t}_{h \min}$ [arrows in Fig. 2(a)], which marks the transition from central fluid drainage to infusion, does not correspond with any immediately observable feature in Figs. 2(b) and 2(c). Specifically, $\hat{t}_{h \min}$ does not occur at the same time as $\hat{t}_{v=0}$.

Restricted fluid infusion into the gap leads to a time lag between the transition from approach to rebound ($\hat{t}_{v=0}$) and the transition from central fluid drainage to infusion ($\hat{t}_{h \min}$). In the elastic half-space limit, for example, when $T = 50$, infusion begins at $\hat{t}_{h \min} \sim 4$, but at that time, both the particle velocity and the coating deformation are already negative [Figs. 2(b) and 2(c)]. Therefore, the spherical particle is closest to the coating when the particle is moving away. During the approach, fluid drainage results in a narrow gap between the particle and coating that restricts infusion at a later time. When the particle is moving away, the narrowness of the fluid gap caused by the curvature of the deformation [inset of Fig. 2(a)] limits the rate of fluid infusion, especially the narrow fluid entry at the edges. Since there is only a finite amount of fluid within the gap and limited fluid infusion into the gap, the particle has to “pull” the soft coating along as it moves away, leading to an almost parallel movement of two surfaces, and ultimately a negative deformation of the soft coating [as illustrated in Fig. 1(b)]. Here, since T affects the compliance of the coating, increasing the coating thickness thereby increases the magnitude of the troughs in Fig. 2(b) (i.e., the maximum distance the particle can pull the soft coating). For a less compliant coating, since the particle can no longer pull the coating before the particle can move away, the fluid has to slowly infuse back into the center of the gap, which thereby limits the rebound velocity of the particle.

The limited fluid infusion into the gap creates a lag between the particle rebound and fluid infusion at the center. For $St = 5$, $\varepsilon = 0.01$, and $T = 50$ (half space), the particle velocity $\hat{v} = v/v_0$ is plotted alongside the fluid gap width in Fig. 3. The gray region starts from $\hat{t}_{v=0}$ to $\hat{t}_{h \min}$, thereby spanning the entire time interval wherein central fluid infusion “lags” behind the particle rebound. The inset shows $\hat{t}_{v=0}$ and $\hat{t}_{h \min}$ for different thickness parameters, and the lag between the two, also highlighted in gray, increases with thickness. For small T , such as $T = 0.05$ in Fig. 3, there is no observable rebound behavior or fluid infusion. Then $\hat{t}_{v=0} \approx \hat{t}_{h \min}$ is the time wherein the sphere simply stops. For $T \sim 0.1$ – 10 , the lag time difference increases, but eventually plateaus at around $T \sim 10$, as the coating thickness is sufficient to match the behavior of the half-space system. Regardless of the thickness parameter, the timescale for elastic rebound is faster than that for fluid infusion.

The dampened oscillations observed in Figs. 2(b) and 2(c) are similar to those observed by Salez and Mahadevan for a cylinder rolling down a ramp with elastic coating [52]. Aside from the central coating deformation [Fig. 2(b)] and velocity [Fig. 2(c)], the central undeformed gap $\hat{x}(0, \hat{t})$ also oscillates, except unlike the prior two which tend toward zero as the oscillations dampen, the central undeformed gap approaches some nonzero equilibrium position \hat{x}_{eq} . In Fig. 3(b) we superimpose the three oscillating curves, $\hat{w}(0, \hat{t})$, $\hat{v}(\hat{t})$, and $\hat{x}(0, \hat{t}) - \hat{x}_{\text{eq}}$, for $St = 5$, $\varepsilon = 0.01$, and $t = 0.05$. The five arrows labeled r_i indicate the i th point where the central deformation (blue curve) crosses the x axis. If the central deformation curve were sinusoidal, the distance between two consecutive r_i would be half the period of the wave. The inset shows the times \hat{t} when each of the three curves crosses the x axis from the first through sixth time. From the inset we note that the three curves share

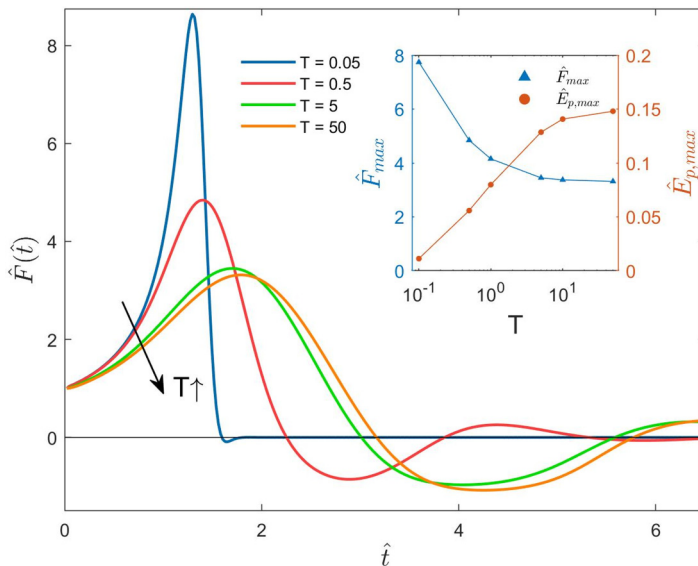


FIG. 4. Hydrodynamic forces during the sphere's approach and rebound. Stokes number and film elasticity are held constant at $St = 5$ and $\varepsilon = 0.01$ while the thickness is changed. Inset: The peak force and the peak stored elastic energy as a function of the coating thickness T .

a similar period of oscillation. How the oscillations vary with Stokes number, elasticity parameter or thickness, or their quantitative predictions are not within the scope of our analysis but would be an interesting topic for future work.

B. Energy analysis

In the previous section, we described the fluid gap and the elastic deformation of the coating at the line of symmetry of the spherical particle. This section focuses on the hydrodynamic forces and macroscopic energy balances during the approach and rebound. The objective is to understand how stratification affects energy dissipation during bouncing.

The thickness parameter affects the scaling of hydrodynamic forces and elastic potential energy. Figure 4 compares the hydrodynamic force, calculated from Eq. (11), for $St = 5$, $\varepsilon = 0.01$, and different thickness parameters. The peak hydrodynamic force and the peak stored potential energy in the coating for different thickness parameters are shown in the inset. We calculate the stored elastic potential energy of the coating using Eq. (12):

$$\hat{E}_p(\hat{t}) = 2\pi \int_0^{0.1\sqrt{a/x_0}} \hat{p}(\hat{r}, \hat{t}) \cdot \hat{w}(\hat{r}, \hat{t}) \hat{r} d\hat{r}. \quad (12)$$

The upper integration limit was based on our mesh boundaries. When we extend the integration limit from $0.1\sqrt{a/x_0}$ to $\sqrt{a/x_0}$, the difference in \hat{E}_p is $<0.1\%$ because the deformation term in the integral is negligible for large \hat{r} .

For all thicknesses the hydrodynamic force reaches a maximum (\hat{F}_{max}) during the approach. As T increases the maximum in the hydrodynamic force occurs later and its magnitude decreases (see Fig. 4). The hydrodynamic force scales directly with the velocity of the spherical particle and inversely with the dimension of the fluid gap between the particle and the coating. As noted in the previous section, coatings with larger thickness parameters are more compliant. Thus, the lubrication pressure from the particle's motion generates a larger deformation in the coating with larger thickness parameter. The larger deformation increases the gap size and decreases the

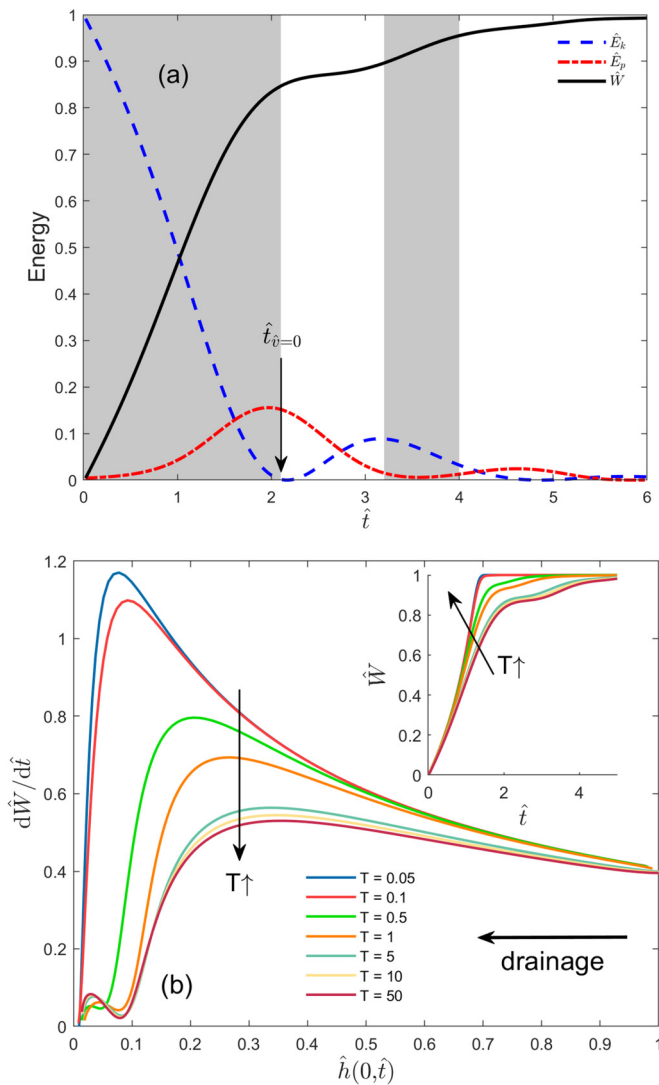


FIG. 5. (a) The particle's kinetic energy (blue dashed line), the coating's stored elastic potential energy (red dot dashed line), and cumulative energy dissipated into the fluid (black solid line) for $T = 50$. The gray and white areas denote the viscous- and elastic-dominated regime, respectively. The Stokes number and elasticity are fixed at $St = 5$ and $\varepsilon = 0.01$. (b) The rate of energy dissipation into the fluid as a function of fluid gap for different thickness parameters. Inset: The time evolution of dissipated energy for different coating thicknesses.

hydrodynamic force. Consequently, the particle decelerates more slowly and takes longer to reach the peak hydrodynamic force, as we observe in Fig. 4. Additionally, the elastic potential energy stored in the coating, as shown in the inset, unsurprisingly increases with T as the magnitude of coating deformation \hat{w} becomes larger for thicker film, especially at the center [Fig. 2(b)].

In the remainder of this section, we discuss the mathematical basis for elastohydrodynamic rebound. Initially, the spherical particle has a finite velocity and kinetic energy and both decrease during the approach toward the soft surface due to the hydrodynamic resistance originating from lubrication pressure. Figure 5(a) below shows the kinetic energy of the particle and the stored elastic potential energy of the coating for $St = 5$, $\varepsilon = 0.01$, and $T = 50$. The stored elastic potential energy

is calculated using Eq. (12) above, while the particle's kinetic energy is calculated using Eq. (13) below:

$$\hat{E}_k = \hat{v}^2. \quad (13)$$

The kinetic energy will reach zero at $\hat{t} = \hat{t}_{v=0}$, marked in Fig. 5(a). At this time, although the kinetic energy is zero, there is elastic potential energy when the coating is deformed. Note that the elastic potential energy peaks before the kinetic energy reaches zero. This is because the relaxation of the coating drives further fluid drainage and generates a lubrication pressure. The hydrodynamic force from the lubrication pressure pushes the spherical particle away from the coating. The kinetic energy is zero when the sphere transitions between approach and rebound. However, as the fluid gap increases between the sphere and the coating, there is a transition from fluid drainage to infusion. From the lubrication equation, the lubrication pressure will be negative (relative to the surrounding fluid pressure). Consequently, the hydrodynamic force is directed downward, pushing the sphere toward the coated surface again, albeit with less momentum. The oscillations observed in Fig. 5(a) originate from the conversion of kinetic energy from the sphere into hydrodynamic force, then into elastic potential energy, and vice versa. The details of this energy conversion process as the basis for elasto-hydrodynamic bouncing are discussed by Davis *et al.* in greater detail (see Ref. [18]).

Although the kinetic energy of the particle is converted into stored elastic potential energy of the soft coating and vice versa, we must also consider nonconservative forces that decrease the efficiency of transfer between these two forms of energy. Similar to a “dry” collision where some energy is transformed into heat in the collision process, in an elasto-hydrodynamic collision, even without contact, the energy is lost through viscous dissipation during fluid drainage and infusion. The dampening of the oscillations in Fig. 5(a) reflects this energy loss through viscous dissipation. We can track the total amount of energy dissipated into the fluid, \hat{W} , through an energy balance:

$$\hat{W} = 1 - \hat{E}_k - \hat{E}_p. \quad (14)$$

The energy dissipated \hat{W} is also shown in Fig. 5(a). Leroy and Charlaix [32] describe the elasto-hydrodynamic interactions of an oscillating, spherical indenter some distance away from an elastic surface using two different regimes: the viscous and elastic regimes. In a viscous-dominated regime, most of the kinetic energy is irreversibly lost through viscous dissipation. The elastic-dominated regime, in contrast, denotes an efficient transfer from kinetic energy to elastic potential energy, and vice versa, with minimal energy dissipation into the fluid. In Fig. 5(a), the particle–soft coating interaction transitions from a viscous-dominated regime (gray) to an elastic-dominated regime ($\hat{t} \sim 2 - 3$) to an intermediate between the two. The viscous regime is characterized by rapid energy dissipation (\hat{W}) through viscous forces, while the elastic regime has little to no energy dissipation, as evidenced by the plateaus of the \hat{W} curve in Fig. 5(a). The width of the fluid gap is one of the factors that determine which regime dominates at a given time [32]. When the fluid gap is large, the resistance to fluid drainage is low. Consequently, the lubrication pressure is lower and the coating will deform less. In this regime, the kinetic energy primarily drives fluid drainage, and the interaction is viscous dominated. As the fluid gap decreases, however, the resistance to fluid drainage is much higher, lubrication pressure increases, and the coating will deform more. As a result, the interaction becomes elastic dominated, and most of the particle's remaining kinetic energy is translated into elastic potential energy, similar to an out-of-contact indentation [36], which is what is observed in Fig. 5(a).

Another factor that determines the relative importance of the elastic- or viscous-dominated regimes is the thickness parameter. Figure 5(b) shows the rate of energy dissipation ($d\hat{W}/d\hat{t}$) at different fluid gap separations, while the particle is approaching the soft coating. As the particle approaches the surfaces, we see that the rate of viscous dissipation increases, and reaches a maximum and then decreases. The decrease after the maximum indicates the transition from viscous-dominated to elastic-dominated regimes also shown in Fig. 5(a) for the limit of an elastic

half space. The curves in Fig. 5(b) clearly show that even at identical fluid gaps the rate of viscous dissipation is higher as the coating thickness decreases. We also see that the transition from viscous-dominated to elastic-dominated regimes shifts to smaller fluid gap distance when the coating thickness decreases. Furthermore, for thin coatings ($T = 0.05$, $T = 0.1$), the approach is only viscous dominated. In this case, $d\hat{W}/d\hat{t}$ will only approach zero when the particle has come to a complete stop. This can be verified by the inset, where the energy dissipation immediately increases from 0 to 1 without reaching a plateau at an intermediate value. The reason smaller thickness parameters increase the rate of energy dissipation is that thinner coatings are less compliant and thus cannot store as much potential energy through deformation, so the kinetic energy is lost through viscous dissipation during the approach.

In summary, we observe that the decrease in compliance caused by stratification increases the viscous dissipation during the collision process (when compared to collisions with an elastic half space of the same elasticity).

C. Critical Stokes number and effective elasticity

We expand our investigation to the effect of coating thickness on the critical Stokes number St_c , defined as the minimum Stokes number for which the particle will rebound away from the coated surface after a collision. Previous theoretical and experimental work on particle rebound demonstrated that surface asperities on the spherical particle or on the substrate allow for physical contact during an elastohydrodynamic collision [24,53,54]. After physical contact is reached, the motion of the particle away from the contact point can be defined as rebound. In the absence of physical contact, as investigated here, the scaling argument can be used to predict rebound. For example, in their work with particles impacting an elastic half space, Davis *et al.* used the condition of $x(0, t) > w(0, t)$ as their criterion for sticking to determine St_c [20]. If at any time the undeformed gap at the center was smaller than the elastic deformation, their predicted outcome was defined as rebound. However, in our case, using a rebound criterion that depends only on the central deformation would lead to errors because the thickness parameter affects the morphology of the deformation profile beyond just the deformation at the centerpoint. See, for example, the inset of Fig. 6, where we compare the deformation profile of coatings for $St = 5$, $\varepsilon = 0.01$ of varying thickness parameters at a selected time \hat{t} . We select the time \hat{t} such that the magnitude of the deformation at the center is similar for all [to emphasize the effect of stratification on the deformation profile, $\hat{w}(\hat{r}, \hat{t})$]; therefore the time \hat{t} is different for different T . (Note that the undulations observed for $T = 0.5$ and $T = 1.0$ are not artifacts of the simulations. In our prior work we directly measured the deformation profile through interferometry and showed the formation of “wimples” or double dimples as those shown in Fig. 6(a) [36].) As the thickness parameter increases, we find that the deformation profile is broader, so more elastic potential energy is available to transform back into kinetic energy for rebound, even if the central deformation is nearly identical. Thus, even after normalizing the central deformation, rebound is more likely to occur if the thickness parameter is larger. This variation is not encompassed by the criterion of Davis *et al.* for the elastic half space. Instead, we propose an alternative rebound criterion that encompasses different thickness parameters: $\hat{v}_r > 0.05$, where \hat{v}_r is the absolute value of the maximum velocity of the particle moving away from the coating.

We plot all our data points that were close to the criterion of Davis *et al.* for rebound in Fig. 6(a). The horizontal dashed line $\hat{x}/\hat{w} = 1$ is their stick-rebound criterion for a half-space model. We selected our stick-rebound criterion for all coating thicknesses as the black vertical dashed line $\hat{v}_r = 0.05$ to minimize the differences of our stick-rebound predictions with that of Davis *et al.* From our criterion, quadrants I and IV are rebound outcomes while quadrants II and III are sticking outcomes. Meanwhile, if we apply their criterion regardless of thickness parameter, quadrants III and IV are rebound outcomes while I and II are sticking outcomes. Most of the results fall within quadrants II and IV regardless of thickness parameter, which shows good consistency between our criterion and that of Davis *et al.* However, several points fall within quadrant III, most of which are situations

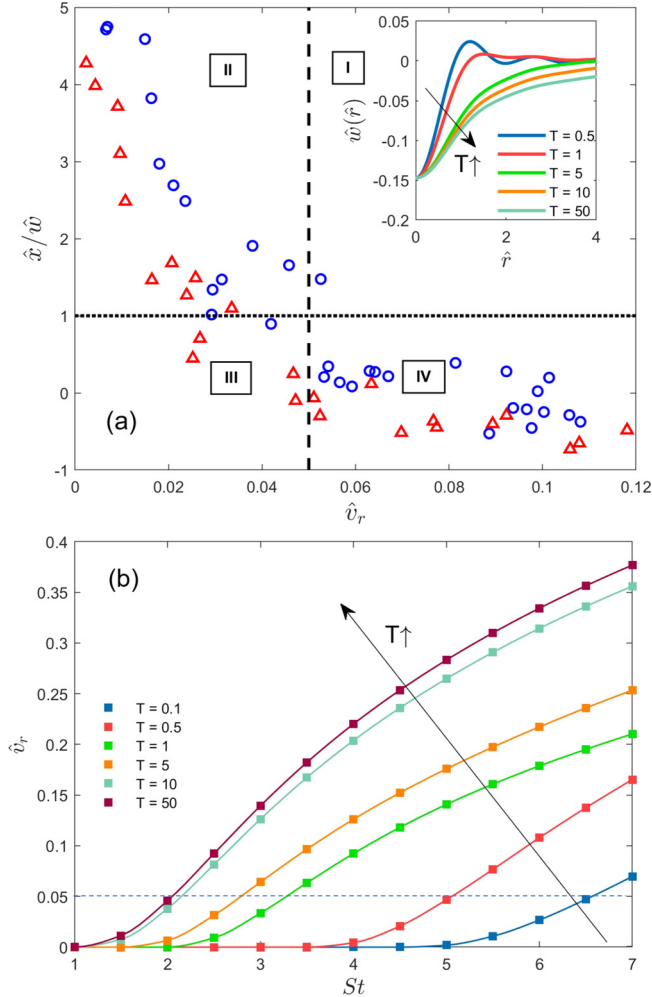


FIG. 6. (a) Comparison between the rebound criterion of Davis *et al.* [20]. (horizontal dotted line) and our own (vertical dashed line). Data points are selected from simulation results with $St = 1 - 7$, $\varepsilon = 0.0001 - 0.01$, $T = 0.05 - 50$ close to the rebound criteria and plotted against the ratio of central undeformed gap (\hat{x}) to deformation (\hat{w}) and the maximum rebound velocity (\hat{v}_r). Red markers indicate small thickness parameters ($T < 1$) while blue markers indicate larger thickness parameters. Based on the criterion of Davis *et al.*, quadrants I and II result in sticking while III and IV are rebound. Based on our criterion, quadrants II and III result in stick while I and IV are rebound. Inset of (a): Cross section of coating deformation for different thicknesses parameters. The time when the deformation is captured is selected specifically to ensure the magnitude of deformation at the center is similar for all T . (b) The maximum rebound velocity (\hat{v}_r) for various Stokes numbers and thickness parameters. Here $\hat{v}_r = v_r/v_0$ can be interpreted as a wet coefficient of restitution. From bottom to top: $T = 0.1, 0.5, 1.0, 5.0, 10$, and 50 . Elasticity parameter was constant at 0.01 . Condition for rebound was set to be a maximum rebound velocity of 0.05 (blue dashed line).

with thickness parameters $T \leq 0.1$, indicated with red markers. As mentioned earlier, even when the central deformation is similar, the likelihood of rebound decreases as coating thickness decreases. As such, the criterion of Davis *et al.* would “overestimate” the rebound for conditions with small thickness parameters, like in quadrant III.

Our proposed rebound criterion allows particles that move a small distance away from the coating after the collision to be considered a nonrebound result. We estimate this distance to be small; we obtain an upper limit of “bouncing” distance for all $St = 1-10$, $\varepsilon = 0.0001-0.01$, and $T = 0.5-50$ surfaces to be 0.015. To give this distance some context, if we consider the sphere to have a radius no more than 0.5 cm, the coating to have a Poisson’s ratio of 0.5, and an elastic modulus between 30 kPa and 5 MPa, the dimensional upper limit of the rebound distance is 100 nm, which is in most cases comparable to or less than the scaling of surface roughness.

Figure 6(b) shows the maximum rebound velocity \hat{v}_r for different Stokes numbers and coating thicknesses. Note here that \hat{v}_r can be interpreted as the wet coefficient of restitution ($COR = \hat{v}_r = v_r/v_0$) [20], except that here the particle is always submerged. As the Stokes number increases, \hat{v}_r first remains nearly constant at a value near to zero before increasing nonlinearly. However, unless there is energy transformation—such as from rotational or chemical to kinetic energy—of which there is none within our conditions, we expect that \hat{v}_r will not exceed 1. The low Re prerequisite limits the range of Stokes numbers that we can test, so we cannot capture the asymptotic behavior of the curve. Nevertheless, we do observe that the curves for rebound velocity for any intermediate thickness are strictly bounded between those of thicker and thinner coatings. Using the rebound criterion \hat{v}_r introduced above, we find the critical Stokes number for different elasticities and thickness parameters.

Prior work by Davis *et al.* [20] and Lian *et al.* [39] relates the St_c of a half space linearly to $\ln(1/\varepsilon)$. Using our rebound criterion, we solve numerically for the critical Stokes number for combinations of elasticities between 0.0001 and 0.05 and coating thicknesses between 0.1 and 50. For each value of the thickness parameter, we observe similar linear relationships between St_c and $\ln(1/\varepsilon)$, as shown in Fig. 7(a). For a coating thickness of 50, which is mechanically equivalent to an elastic half space, we find that $St_c = 0.64 \ln(1/\varepsilon) - 0.89$. The difference in our equation compared to those of Davis *et al.* $St_c = 0.40 \ln(1/\varepsilon) - 0.20$ and Lian *et al.*, $St_c = 0.52 \ln(1/\varepsilon) - 1.67$, is due to the rebound criterion used. Compared to the other two St_c equations, ours will yield slightly higher values of St_c for the same elasticity parameter.

In Fig. 7(a), we also show that the linear relationship between St_c and $\ln(1/\varepsilon)$ holds for thin and intermediate coatings just like the case of the half space, but with different slope and y intercept of the line. Also shown are the prediction from Davis *et al.* [20] and Lian *et al.* [39] for comparison. From the variation in slope, we observe that coating thickness moderates the sensitivity of the critical Stokes number to elasticity. In other words, for the same change in elasticity, the critical Stokes number of a thinner coating will change less than a thicker coating. Similarly, for the same change in the thickness parameter, the critical Stokes number will change more significantly when $\ln(1/\varepsilon)$ is smaller; i.e., the coating material is softer. The reason for both of these trends is the sensitivity of compliance to both ε and T . Large changes in ε will result in smaller changes in compliance when T is small, and vice versa.

To further quantify the role of coating thicknesses on critical Stokes number St_c , we summarize our results in Fig. 7(a) for intermediate to thick coating thickness T and rewrite the equation for the critical Stokes number in the form

$$St_c = \alpha(T) \ln\left(\frac{1}{\varepsilon}\right) + \beta(T). \quad (15)$$

Note that $\alpha(T)$ and $\beta(T)$ are sole functions of coating thickness (geometrical constraint) which is fully decoupled from the material property in Eq. (15). To obtain the functional forms for $\alpha(T)$ and $\beta(T)$ for Eq. (15), 250 trials with $T = 0.1-50$ were fitted using MATLAB’S CFTOOL. For $\beta(T)$ we interpolate the numerical results to the (unphysical) limit of $\ln(1/\varepsilon) = 0$ [shown in dashed lines in Fig. 7(a)]. The only limitation was that $\alpha(T)$ and $\beta(T)$ approach the thick coating asymptotic value of $\alpha(\infty) = 0.64$ and $\beta(\infty) = -0.89$, respectively. Negative values for $\beta(\infty)$ have been predicted by others [20,39]. Within the parameter space investigated here ($\varepsilon < 0.01$), the negative values for β never lead to negative St_c . It is possible that Eq. (15) would no longer be linear for values of

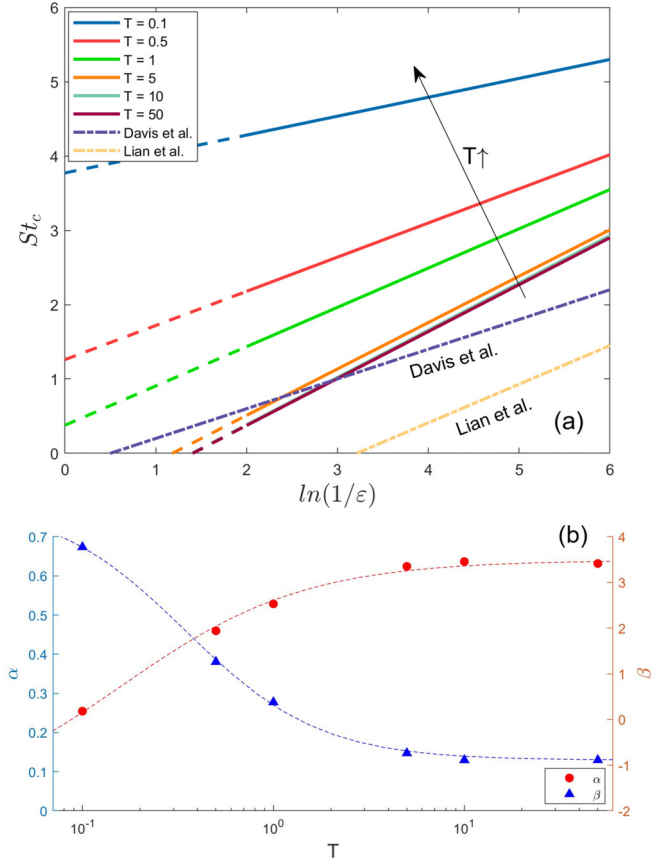


FIG. 7. (a) Critical Stokes St_c as a linear function of $\ln(1/\epsilon)$ for different thickness parameters. From top to bottom, $T = 0.1, 0.5, 1, 5, 10, 50$. Also shown are the predictions from Davis *et al.* [18] and Lian *et al.* [37] for comparison. Dashed lines are extrapolated from a linear fit of the data at $\ln(1/\epsilon) \geq 2$. (b) Slope α [Eq. (16)] and y intercept β [Eq. (17)] of the St_c equation [Eq. (15)], as functions of the thickness parameter T . The circular and triangular markers are values of slope and y intercept, respectively, from Fig. 8(a), while the dotted lines are curve fits generated using MATLAB CFTOOL.

the elasticity parameter beyond the range investigated in our work. The resulting curve fits are as follows:

$$\alpha(T) = \frac{0.64}{1 + 0.19T^{-0.91}}, \quad (16)$$

$$\beta(T) = 4.76 - \frac{5.65}{1 + 0.27T^{-1.24}}. \quad (17)$$

The two equations are a good fit for the $\alpha(T)$ and $\beta(T)$ data points, as shown in Fig. 7(b) above. At intermediate thickness parameters, $0.1 < T < 1$, the values of $\alpha(T)$ and $\beta(T)$ are increasing and decreasing, respectively. Increasing $\alpha(T)$ corresponds to an increased sensitivity of St_c in response to changes in elasticity. Both curves begin to plateau at $T > 10$, where the thickness parameter is significantly large to be comparable to an elastic half space. On the other hand, since there was limited data for rebound in thin coating parameter conditions $T < 0.1$, the behavior of Eqs. (16) and (17) in that region are not accurate. In the theoretical limiting case of an extremely thin coating $T \rightarrow 0$, the compliance of the coating is essentially that of the rigid substrate regardless of the

elasticity of the coating. We would expect that under those conditions, the St_c is insensitive to changes in the elasticity parameter, so $\alpha(0) = 0$, which is satisfied by Eq. (16). On the other hand, the extremely thin coating, which will be as noncompliant as the rigid substrate, will not be able to deform and store elastic potential energy. Thus, assuming that there are no surface asperities on the particle, all the kinetic energy of the particle will be dissipated through fluid drainage, and there will not be any rebound. There is no value of St that can cause the particle to rebound away from the coating, so theoretically, $\beta(0) = \infty$. This is not the case in Eq. (17), where the asymptotic value of β as $T \rightarrow 0$ is 4.76. The consequence of this is that our equation would underestimate the value of St_c for thin coatings.

In the next sections, we propose an effective elasticity parameter that combines both thickness and elasticity parameters to predict St_c . The rationale is that a coating of some thickness and elasticity parameters might behave similarly to a different coating with another set of thickness and elasticity parameters. The linearity of Eq. (15) allows us to solve for different pairs of elasticity and coating thickness that yield the same critical Stokes number. As long as $\alpha(T)$ is nonzero, then for every St_c , there are infinitely many pairs of ε and T that will satisfy the equation. For the unique case that the coating is a half space ($T \sim \infty$), we define the elasticity that yields that specific St_c to be the “effective” elasticity ε' . The effective elasticity is defined such that a soft coating with some finite thickness and elasticity will have the same critical Stokes number as a half space of that given effective elasticity. It is important to remember that other than the St_c , the finite coating thickness system and the effective elasticity half-space system will not share similar deformation profiles, drainage time, separation, or other variables. However, there is still merit to relying on an effective elasticity for the St_c since for large-scale collision models and simulations, St_c is one of the most important parameters as it can be used to calculate the postcollision rebound velocity of particles rapidly.

To solve for the effective elasticity for any pair of ε and T , we rearrange Eq. (15) as

$$\varepsilon' = \varepsilon^{\alpha'(T)} \exp[\beta'(T)], \quad (18)$$

where $\alpha'(T) = \alpha(T)/\alpha(\infty)$ and $\beta'(T) = [\beta(\infty) - \beta(T)]/\alpha(\infty)$. As noted previously, for a half space, the slope $\alpha(\infty)$ and intercept $\beta(\infty)$ are 0.64 and -0.89 , respectively. The same limitations for Eqs. (16) and (17) also hold here, specifically the loss of accuracy for $T < 0.1$.

Figure 8(a) shows a contour plot that shows pairs of the thickness and elasticity parameters that yield the same effective elasticity parameter based on Eq. (18). The effective elasticity increases with coating thickness or elasticity. Note that above a certain coating thickness, around $T \sim 10$ or so, the effective elasticity no longer changes with T . Beyond that point, $\varepsilon' \sim \varepsilon$, and the thickness parameter is large enough to be equivalent to a half space. However, the exact value of T past which the effective elasticity no longer changes is not constant. As shown in Fig. 8(a), as the elasticity parameter increases, that half-space approximation T threshold increases as well. This changing threshold would be of significance to determine whether it is valid to assume that a given coating is thick enough to be treated as an elastic half space.

We verify our equation for the effective elasticity against data from 250 simulations with different Stokes number, elasticity, and coating thickness parameters. For each unique triplet St , ε' , and T , we calculate the effective elasticity ε' and verify if the rebound velocity is above the threshold for bouncing. First, since the elasticity of a half space is equivalent to its effective elasticity, Eq. (18) below shows the critical Stokes number as a function of effective elasticity.

$$St_c = 0.64 \ln \left(\frac{1}{\varepsilon'} \right) - 0.89. \quad (19)$$

Figure 8(b) includes this line to separate the bouncing and sticking outcomes. Then in Fig. 8(b), we assign a different marker depending on whether or not the results of the simulation for the (St, ε') pair matched the rebound criterion. If the result matched the criterion, a red circular marker was assigned, with a filled marker indicating a sticking outcome, and an empty marker indicating a

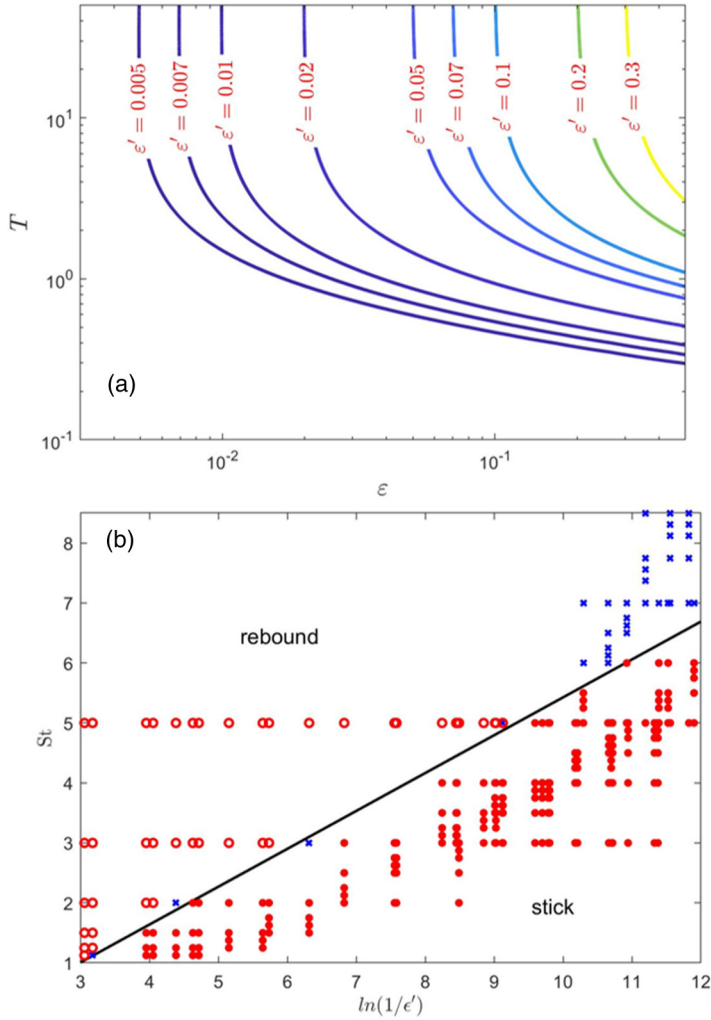


FIG. 8. (a) Contour plot showing the effective elasticity (ϵ') for different T and ϵ values. Every point on the same contours indicates that this combination of T and ϵ yields the same effective elasticity value, indicated in red at the upper portion of the figure. (b) Verification of proposed effective elasticity formula. Results from trials with different combinations of Stokes number and effective elasticity are shown with different markers. The red filled circular markers and the red empty circular markers denote sticking and rebound outcomes, respectively, in the data sets, both of which match our rebound criterion. The blue “x” markers denote data that do not fit the stick-rebound criterion proposed.

rebound outcome. On the other hand, if the result did not match the criterion, a blue “x” marker was assigned to the data point. From Fig. 8(b), for most combinations of (St, ϵ') , Eq. (19) separates the sticking cases and the bouncing cases successfully, meaning that it can be used directly to determine whether the particle will stick or rebound. For an experimental design with combination of coating thickness and material property, one can simply use Eq. (18) to calculate the effective elasticity, and use Eq. (19) to find the critical Stokes number—the minimum Stokes number needed for a rebound to occur. However, we observe that a large cluster of data points on the upper-right corner did not match the stick-rebound criterion. In fact, when $\ln(1/\epsilon') > 10$, all the data points indicate that the particle did not rebound. The cluster of data points not captured by the effective elasticity is due

to the choice of $\beta(T)$. In the limit of $T \rightarrow 0$, $\beta(T)$ should approach infinity so that the effective elasticity approaches zero (equivalent to a rigid half space). However, since our arbitrary choice of $\beta(T)$ does not reach infinity, the effective elasticity is less accurate when $T < 0.1$. To address this, we can modify the stick-rebound criterion in Eq. (19) to also include this additional restriction.

IV. CONCLUSIONS

We rescaled the equations governing the elasto-hydrodynamic collision of a rigid sphere against a rigid, planar substrate with a soft incompressible coating of finite thickness. The rescaling showed that an additional thickness parameter is also necessary to describe the collisions (besides the Stokes number and elasticity parameter that were already previously employed). The thickness parameter was shown to affect the degree to which the compliance of the soft coating was similar to that of the rigid substrate. We then developed bouncing criteria for the stratified substrate, characterized by the critical Stokes number (St_c). We find that St_c decreases when either the thickness parameter increases, or the elasticity parameter decreases. We then obtain a closed form correction for an effective elasticity that accounts for the effect of stratification for the St_c . The correction can be employed along existing classic scaling of St_c , without the need of full numerical simulations. By coupling thickness and elasticity parameters into effective elasticity, the original elasto-hydrodynamic bouncing problem is simplified as the dependency on three dimensionless parameters is reduced to only two (St and ε). The method we developed in this article can be used to improve the accuracy of large-scale multiparticle simulations, which are currently limited to the dichotomous “hard sphere” or “soft sphere” types of particles, with no option for stratified materials. We also provide regime maps that can be employed to predict rebound or sticking after normal collisions. These different regimes are crucial for understanding some non-Newtonian behavior of highly concentrated particulate systems [42,43].

ACKNOWLEDGMENTS

This work was supported by the National Science Foundation through NSF-CMMI Grant No. 1538003 and through a Research Experience for Undergraduate Supplement for M.R.T. M.R.T. also acknowledges support from the Johns Hopkins University Provost Undergraduate Research Award (PURA). Y.W. also acknowledges support from the National Natural Science Foundation of China (Grant No. 51804319) and the Science Foundation of China University of Petroleum, Beijing (Grant No. 2462018YJRC002).

-
- [1] Z. Adamczyk, K. Sadlej, E. Wajnryb, M. Nattich, M. L. Ekiel-Jeżewska, and J. Bławzdziejewicz, Streaming potential studies of colloid, polyelectrolyte and protein deposition, *Adv. Colloid Interface Sci.* **153**, 1 (2010).
 - [2] C. B. Solnordal, Y. W. Chong, and J. Boulanger, An experimental and numerical analysis of erosion caused by sand pneumatically conveyed through a standard pipe elbow, *Wear* **336-337**, 43 (2015).
 - [3] R. A. Bagnold, Experiments on a gravity-free dispersion of large solid spheres in a Newtonian fluid under shear, *Proc. R. Soc. London* **225**, 49 (1954).
 - [4] H. M. Jaeger, S. R. Nagel, and R. P. Behringer, Granular solids, liquids, and gases, *Rev. Mod. Phys.* **68**, 1259 (1996).
 - [5] Y. M. Chen, Recent advances in FCC technology, *Powder Technol.* **163**, 2 (2006).
 - [6] M. P. Dudukovic, Frontiers in reactor engineering, *Science* **325**, 698 (2009).
 - [7] C. T. Yavuz, A. Prakash, J. T. Mayo, and V. L. Colvin, Magnetic separations: From steel plants to biotechnology, *Chem. Eng. Sci.* **64**, 2510 (2009).

- [8] Y. Lu, Z. Huang, R. Hoffmann, L. Amundsen, and H. S. Fogler, Counterintuitive effects of the oil flow rate on wax deposition, *Energy Fuels* **26**, 4091 (2012).
- [9] K. S. Soppimath, T. M. Aminabhavi, A. R. Kulkarni, and W. E. Rudzinski, Biodegradable polymeric nanoparticles as drug delivery devices, *J. Controlled Release* **70**, 1 (2001).
- [10] D. A. Fedosov, W. Pan, B. Caswell, G. Gompper, and G. E. Karniadakis, Predicting human blood viscosity in silico, *Proc. Natl. Acad. Sci. USA* **108**, 11772 (2011).
- [11] Y. Li and E. Kumacheva, Hydrogel microenvironments for cancer spheroid growth and drug screening, *Sci. Adv.* **4**, eaas8998 (2018).
- [12] F. Wu, S. Chen, B. Chen, M. Wang, L. Min, J. Alvarenga, J. Ju, A. Khademhosseini, Y. Yao, Y. S. Zhang *et al.*, Bioinspired universal flexible elastomer-based microchannels, *Small* **14**, 1702170 (2018).
- [13] A. Pandey, S. Karpitschka, C. H. Venner, and J. H. Snoeijer, Lubrication of soft viscoelastic solids, *J. Fluid Mech.* **799**, 433 (2016).
- [14] J. H. Snoeijer, Analogies between elastic and capillary interfaces, *Phys. Rev. Fluids* **1**, 060506 (2016).
- [15] Y. Wang, G. A. Pilkington, C. Dhong, and J. Frechette, Elastic deformation during dynamic force measurements in viscous fluids, *Curr. Opin. Colloid Interface Sci.* **27**, 43 (2017).
- [16] Y. Wang, C. Dhong, and J. Frechette, Out-of-Contact Elastohydrodynamic Deformation Due to Lubrication Forces, *Phys. Rev. Lett.* **115**, 248302 (2015).
- [17] P. Gondret, M. Lance, and L. Petit, Bouncing motion of spherical particles in fluids, *Phys. Fluids* **14**, 643 (2002).
- [18] R. H. Davis, J.-M. Serayssol, and E. J. Hinch, The elastohydrodynamic collision of two spheres, *J. Fluid Mech.* **163**, 479 (1986).
- [19] G. Barnocky and R. H. Davis, Elastohydrodynamic collision and rebound of spheres: Experimental verification, *Phys. Fluids* **31**, 1324 (1988).
- [20] R. H. Davis, D. A. Rager, and B. T. Good, Elastohydrodynamic rebound of spheres from coated surfaces, *J. Fluid Mech.* **468**, 107 (2002).
- [21] K. Apostolou and A. N. Hrymak, Discrete element simulation of liquid-particle flows, *Comput. Chem. Eng.* **32**, 841 (2008).
- [22] H. P. Zhu, Z. Y. Zhou, R. Y. Yang, and A. B. Yu, Discrete particle simulation of particulate systems: A review of major applications and findings, *Chem. Eng. Sci.* **63**, 5728 (2008).
- [23] P. Gondret, E. Hallouin, M. Lance, and L. Petit, Experiments on the motion of a solid sphere toward a wall: From viscous dissipation to elastohydrodynamic bouncing, *Phys. Fluids* **11**, 2803 (1999).
- [24] G. G. Joseph, R. Zenit, M. L. Hunt, and A. M. Rosenwinkel, Particle-wall collisions in a viscous fluid, *J. Fluid Mech.* **433**, 329 (2001).
- [25] G. G. Joseph and M. L. Hunt, Oblique particle-wall collisions in a liquid, *J. Fluid Mech.* **510**, 71 (2004).
- [26] R. Zenit and M. L. Hunt, Mechanics of immersed particle collisions, *J. Fluids Eng.* **121**, 179 (1999).
- [27] T. Müller and K. Huang, Influence of the liquid film thickness on the coefficient of restitution for wet particles, *Phys. Rev. E* **93**, 042904 (2016).
- [28] T. Chastel, P. Gondret, and A. Mongruel, Texture-driven elastohydrodynamic bouncing, *J. Fluid Mech.* **805**, 577 (2016).
- [29] H. Ow, D. R. Larson, M. Srivastava, B. A. Baird, W. W. Webb, and U. Wiesner, Bright and stable core-shell fluorescent silica nanoparticles, *Nano Lett.* **5**, 113 (2005).
- [30] K. Volk, J. P. S. Fitzgerald, M. Retsch, and M. Karg, Time-controlled colloidal superstructures: Long-range plasmon resonance coupling in particle monolayers, *Adv. Mater.* **27**, 7332 (2016).
- [31] T. J. Baudouin Saintyves, T. Salez, and L. Mahadevan, Self-sustained lift and low friction via soft lubrication, *Proc. Natl. Acad. Sci. USA* **113**, 5847 (2016).
- [32] S. Leroy and E. Charlaix, Hydrodynamic interactions for the measurement of thin film elastic properties, *J. Fluid Mech.* **674**, 389 (2011).
- [33] F. Restagno, E. Martinot, R. Villey, S. Leroy, C. Poulard, E. Charlaix, and L. Léger, Sensing the mechanical properties of supported micro-to nano-elastic films, in *Handbook of Nanomaterials Properties* (Springer, Berlin, Heidelberg, 2014), pp. 575–614.
- [34] N. Balmforth, C. Cawthorn, and R. Craster, Contact in a viscous fluid. Part 2. A compressible fluid and an elastic solid, *J. Fluid Mech.* **646**, 339 (2010).

- [35] Y. Wang, M. R. Tan, and J. Frechette, Elastic deformation of soft coatings due to lubrication forces, *Soft Matter* **13**, 6718 (2017).
- [36] Y. Wang and J. Frechette, Morphology of soft and rough contact via fluid drainage, *Soft Matter* **14**, 7605 (2018).
- [37] J. Li and T.-W. Chou, Elastic field of a thin-film/substrate system under an axisymmetric loading, *Int. J. Solids Struct.* **34**, 4463 (1997).
- [38] T. Nogi and T. Kato, Influence of a hard surface layer on the limit of elastic contact—Part I: Analysis using a real surface model, *J. Tribol.* **119**, 493 (1997).
- [39] G. Lian, M. J. Adams, and C. Thornton, Elastohydrodynamic collisions of solid spheres, *J. Fluid Mech.* **311**, 141 (1996).
- [40] E. Izard, T. Bonometti, and L. Lacaze, Modelling the dynamics of a sphere approaching and bouncing on a wall in a viscous fluid, *J. Fluid Mech.* **747**, 422 (2014).
- [41] L. C. Hsiao, S. Jamali, E. Glynos, P. F. Green, R. G. Larson, and M. J. Solomon, Rheological State Diagrams for Rough Colloids in Shear Flow, *Phys. Rev. Lett.* **119**, 158001 (2017).
- [42] X. Cheng, J. H. McCoy, J. N. Israelachvili, and I. Cohen, Imaging the microscopic structure of shear thinning and thickening colloidal suspensions, *Science* **333**, 1276 (2011).
- [43] N. J. Wagner and J. F. Brady, Shear thickening in colloidal dispersions, *Phys. Today* **62**(10), 27 (2009).
- [44] C. B. Holmes, M. E. Cates, M. Fuchs, and P. Sollich, Glass transitions and shear thickening suspension rheology, *J. Rheol.* **49**, 237 (2005).
- [45] E. Gacoin, C. Fretigny, A. Chateauminois, A. Perriot, and E. Barthel, Measurement of the mechanical properties of thin films mechanically confined within contacts, *Tribol. Lett.* **21**, 245 (2006).
- [46] S. Pathak and S. R. Kalidindi, Spherical nanoindentation stress–strain curves, *Mater. Sci. Eng., R* **91**, 1 (2015).
- [47] F. Gollwitzer, I. Rehberg, C. A. Kruehle, and K. Huang, Coefficient of restitution for wet particles, *Phys. Rev. E* **86**, 011303 (2012).
- [48] A. Gopinath and L. Mahadevan, Elastohydrodynamics of wet bristles, carpets and brushes, *Proc. R. Soc. A* **467**, 1665 (2011).
- [49] G. N. Greaves, A. Greer, R. Lakes, and T. Rouxel, Poisson’s ratio and modern materials, *Nat. Mater.* **10**, 823 (2011).
- [50] See Supplemental Material at <http://link.aps.org/supplemental/10.1103/PhysRevFluids.4.084305> for animation that compares the approach, deformation, and rebound for the four particular thickness parameters: $T = 0.05, 0.5, 5,$ and 50 .
- [51] V. M. Kulik, S. V. Rodyakin, I. Lee, and H. H. Chun, Deformation of a viscoelastic coating under the action of convective pressure fluctuations, *Exp. Fluids* **38**, 648 (2005).
- [52] T. Salez and L. Mahadevan, Elastohydrodynamics of a sliding, spinning and sedimenting cylinder near a soft wall, *J. Fluid Mech.* **779**, 181 (2015).
- [53] J. R. Smart and D. T. Leighton, Measurement of the hydrodynamic surface roughness of noncolloidal spheres, *Phys. Fluids* **1**, 52 (1989).
- [54] S. K. Birwa, G. Rajalakshmi, R. Govindarajan, and N. Menon, Solid-on-solid contact in a sphere-wall collision in a viscous fluid, *Phys. Rev. Fluids* **3**, 044302 (2018).